Intrinsic Predictability Limits arising from Indian Ocean MJO Heating: Effects on tropical and extratropical teleconnections

David M. Straus[1], Daniela I.V. Domeisen[3,4], Sarah-Jane Lock[2], Franco Molteni[2], and Priyanka Yadav[4]

[1]Center for Ocean-Land-Atmosphere Studies, George Mason University, Fairfax, VA, USA
[2]European Centre for Medium-Range Forecasts, Reading, UK
[3]University of Lausanne, Lausanne, Switzerland
[4]Institute for Atmospheric and Climate Science, ETH Zurich, Zurich, Switzerland
Correspondence: David Straus (dstraus@gmu.edu)

Abstract. Since the Madden-Julian Oscillation (MJO) is a major source for tropical and extratropical variability on weekly to monthly timescales, the intrinsic predictability of its global teleconnections is of great interest. As the tropical diabatic heating associated with the MJO ultimately drives these teleconnections, the effect of the variability of heating among various episodes of the same MJO phase will limit this predictability. In order to assess this limitation, a suite of 60-day ensemble reforecasts

5 has been carried out with the ECMWF forecast model, spanning 13 starting dates from 01Nov and 01Jan for different years. The initial dates were chosen so that phases 2 and 3 of the MJO (with anomalous tropical heating in the Indian Ocean sector) were present in the observed initial conditions. The 51 members of an individual ensemble use identical initial conditions for the atmosphere and ocean. Stochastic perturbations to the tendencies produced by the atmospheric physics parameterizations are applied only over the Indian Ocean region. This guarantees that the spread between reforecasts within an ensemble is

10 due to perturbations in heat sources only in the Indian Ocean sector. The point-wise spread in the intra-ensemble (or error) variance of vertically integrated tropical heating Q is larger than the average ensemble mean signal even at early forecast times; however the planetary wave component of Q (zonal waves 1-3) is predictable for 24 days for 01Nov starts and 28 days for 01Jan starts. The predictability times, measured by the time at which the error variance reaches 0.5 of its saturation value, decreases to 18-20 days for zonal waves 4-10, and 14 days for waves 11-21. In contrast, the planetary wave component of

15 the 200 hPa Rossby wave source, which is responsible for propagating the influence of tropical heating to the extratropics, is only predictable for 14 to 19 days, very close to the predictability times for the 200 hPa vorticity in the $40^o N - 50^o N$ latitude belt. In terms of geographical distribution, substantial ensemble spread of heating and 200 hPa vorticity propagates from the tropics to the Northern Hemisphere storm-track regions by days 15-16. Following the growth of upper tropospheric spread in planetary wave heat flux, the stratosphere provides a feedback in enhancing the error via downward propagation towards the

20 end of both Nov. and Jan. reforecasts.

1 Introduction

The Madden-Julian Oscillation (Madden and Julian, 1971, 1972) is the dominant mode of tropical variability on subseasonal timescales of several weeks. The MJO manifests as a large-scale convection and precipitation pattern that starts in the Indian

ocean, followed by an eastward propagation along the equator. Although the MJO itself is confined to the tropics, it can
influence a large part of the globe, including the extratropics, through a wide range of remote impacts, so-called teleconnections
(Stan et al., 2017). The best documented teleconnections include impacts on tropical cyclones (Maloney and Hartmann, 2000;
Camargo et al., 2019; Hall et al., 2001; Camargo et al., 2009), the North Pacific (Wang et al., 2020), North America (Lin and
Brunet, 2009), South America (Valadão et al., 2017), the North Atlantic region (Cassou, 2008; Lin et al., 2009), as well as the
upper atmosphere over the Northern hemisphere polar regions (Garfinkel et al., 2014). The mechanisms for an MJO influence
on global weather and climate act through the propagation of Rossby waves that are triggered by the diabatic heating anomalies
associated with the MJO convection (Sardeshmukh and Hoskins, 1988).

MJO teleconnections are a major source of predictability on sub-seasonal to seasonal timescales around the globe (Vitart,
2017; Merryfield et al., 2020; Stan et al., 2022), including for tropical cyclones (Leroy and Wheeler, 2008; Lee et al., 2018;
Domeisen et al., 2022), extreme precipitation (Jones et al., 2004; Muñoz et al., 2016), temperature in North America (Rodney
et al., 2013), and the Northern Hemisphere stratosphere (Garfinkel and Schwartz, 2017), which in turn can have a strong
downward impact on surface weather in the extratropics (Baldwin and Dunkerton, 2001), with strong impacts on extratropical
sub-seasonal predictability (Domeisen et al., 2020a).

One class of well-studied teleconnections is that associated with the phase of the MJO with enhanced convection over the
Indian Ocean (MJO phases 2 and 3), which tends to be associated with a positive phase of the North Atlantic Oscillation
(NAO) (Lin et al., 2009; Ferranti et al., 1990; Cassou, 2008; Straus et al., 2015) roughly 1-2 weeks later, leading to added
predictability (Lin et al., 2010; Vitart, 2014). The teleconnection of the MJO variability to the NAO is however also modulated
by El Niño-Southern Oscillation (Lee et al., 2019), by the propagation speed of the MJO (Yadav and Straus, 2017), and by the
strength of the Northern Hemisphere stratospheric polar vortex (Garfinkel and Schwartz, 2017).

Limits to the predictability of MJO teleconnections are due to both the model errors, such as basic state bias (Schwartz and
Garfinkel, 2020; Garfinkel et al., 2022; Stan et al., 2022) and the presence of baroclinic instability and non-linear extratropical
interactions. However, there are potential additional limits imposed by the uncertainty in MJO heating, as witnessed by the
variability in the details of heating among different episodes of a given phase. In fact, the wealth of MJO teleconnection
research discussed above has relied almost exclusively on the Wheeler-Hendon multivariate empirical orthogonal function
framework (Wheeler and Hendon, 2004). This framework, by design, involves both spatial smoothing and coarse-graining of
the temporal and longitudinal fields of zonal wind and outgoing long-wave radiation, the latter as a proxy for precipitation and
thus diabatic heating. Much less studied are the effects on the MJO teleconnections due to the intermittency and variability of
the MJO diabatic heating itself.

The purpose of this paper is to assess the intrinsic limits of potential predictability due to this uncertainty. We approach this
using large forecast ensembles of a global model that simulates the MJO reasonably well (as described in Section 2), and so
make the "perfect model" assumption that the errors in the model do not substantially invalidate our findings. To this end a
series of unique ensemble reforecasts have been carried out that are specifically designed to diagnose the uncertainty in both
the tropics and the extratropics that arises due to the high degree of space/time intermittency of diabatic heating within phases
2 and 3 of the MJO. In these reforecasts made with the Integrated Forecast System (IFS) of the European Centre for Medium-

Range Forecasts (ECMWF), the stochastic parametrization scheme (SPPT) described in Leutbecher et al. (2017) has been

60 altered so that perturbations which affect (directly or indirectly) diabatic heating tendencies are confined to the tropical Indian Ocean region. Since all members of each ensemble use the identical initial conditions, the only cause of model uncertainty (also called error here) must be the noise in heating introduced by the SPPT in the tropical Indian Ocean.

Since our goal is to document both the uncertainty in the tropical heating and the mid-latitude response in these experiments, we also consider the pathway by which the tropical heating forces extratropical Rossby waves. Although the MJO-related

65 tropical heating is expected to force a corresponding signal in upper tropospheric divergence, this signal generally occurs within an easterly background wind, where stationary Rossby waves are not expected to propagate. Sardeshmukh and Hoskins (1988) derive a more complete formulation of the source of barotropic Rossby waves which involves the advection of the absolute vorticity by the divergent component of the flow, and importantly acts in the vicinity of the sub-tropical jet, and so in a background of westerlies. Although strictly speaking the response to the MJO is not stationary, previous success in explaining

70 the extratropical response in terms of stationary wave theory (e.g. Matthews et al., 2004) suggests that stationary wave concepts are relevant here.

Section 2 describes the model and ensemble reforecast experiments in detail, as well as the methods used to diagnose the results. The signal and uncertainty in the tropical heating, Rossby wave source, and circulation on various spatial scales are described in Section 3, along with the signal and uncertainty in the Rossby Wave Source. Section 4 describes the global spread

75 of error in the heating and circulation and its scale-dependence, while Section 5 shows results related to the stratospheric involvement. The Discussion is given in Section 6, and Conclusions in Section 7.

2 Methods and Data

This section introduces the data used in this study, the model experiments performed for this study, and the metrics used to evaluate the data.

80 ### 2.1 Model configuration

This study has been performed using ensemble forecast experiments with the ECMWF Integrated Forecasting System (IFS Cy43r3: see ECMWF (2017a)). The IFS is a global earth system model, which includes an atmospheric numerical weather prediction model coupled to ocean, sea-ice, ocean waves and land surface models. The experiments have been run with the ensemble forecasting system ("ENS") close to the configuration used operationally for the ECMWF extended-range forecasts

85 (https://www.ecmwf.int/en/forecasts/documentation-and-support/extended-range-forecasts). This configuration has an atmospheric model resolution of TCo319L91 (approximately 36 km horizontal grid spacing, with 91 vertical levels up to 0.01 hPa, with a timestep of 1200s), coupled to the NEMO ocean model v3.4.1 (Madec and the NEMO team, 2013) in the ORCA025_Z75 configuration (1/4 degree horizontal resolution, 75 vertical levels), the LIM2 sea-ice model (Goosse and Fichefet, 1999) and the ECMWF Wave Model (ecWAM ECMWF, 2017b). The model system used here is strongly related to the ECMWF extended-

90 range prediction system used for subseasonal to seasonal (S2S) forecasts that is included in the S2S prediction project database

(Vitart et al., 2017). This prediction system has been systematically evaluated for its ability to represent MJO teleconnections, along with other prediction systems from the S2S database (Vitart et al., 2017; Stan et al., 2022). Overall, the ECMWF system reproduces a realistic teleconnection to the Northern Hemisphere, though with a too weak amplitude. Among the models investigated in the above studies, the ECMWF system exhibits a skillful representation of the MJO teleconnections. Hence using the ECMWF system to study error growth from MJO teleconnections allows for an identification of remaining issues at a state-of-the-art level of model development.

2.2 Description of ensemble reforecasts

Ensemble reforecasts were made for initial dates of 01 Nov and 01 Jan, but only for those years (between 1981 and 2016) when the MJO resided in phases 2 or 3 with an amplitude greater than 1.0 on the initial date. From the MJO amplitude and phase data from the Australian Bureau of Meterology (http://www.bom.gov.au/climate/mjo/), this condition yielded eight years for the Nov reforecasts and five for the Jan reforecasts. The dates are given in Table 1.

All members of each ensemble forecast are initialized with *identical* initial conditions from the ERA-Interim reanalysis data (Dee and coauthors, 2011). There are no perturbations applied to the initial conditions. The control forecast for each initial date also has no perturbations applied during the integration. The 50 additional members of each ensemble forecast differ only in that perturbations are applied during the model integrations. These are introduced via the operational model uncertainty scheme, SPPT (Stochastically Perturbed Parametrization Tendencies scheme, see Leutbecher et al., 2017; Buizza et al., 1999). SPPT is designed to represent model uncertainty due to the parameterization of atmospheric physical processes. In ECMWF's operational forecasts, SPPT perturbations are applied at every time step of the runs and at every grid-point over the entire globe. However, for these experiments, a mask is applied such that the SPPT perturbations are only active within a window over the Indian Ocean, i.e. they are fully active in $(50E - 120E, 20N - 20S)$ and tapered to zero within the neighbouring 5 degrees (in all directions). All the forecasts are run to a lead-time of 60 days.

In addition, 01 Nov and 01 Jan ensemble reforecasts were made for all years between 1981 and 2016 with the initial dates of 01 Nov and 01 Jan. Here the ensemble size is 9, with a control (unperturbed) run and 8 perturbed runs. The purpose of these 'all-year' reforecasts is to establish the model reforecast seasonal cycle for the Nov-Dec and Jan-Feb periods. Table 1 summarizes the MJO and all-year reforecasts, while Table 2 gives the MJO amplitude and phase for each of the reforecasts of Table 1. In addition, Table 2 gives the monthly mean Niño 3.4 indices to indicate the state of the El-Niño Southern Oscillation. (This index is defined as the sea-surface temperature averaged over the region $5^o - 5^o N$ and $170^o W - 120^o W$, and was obtained from the website https://www.cpc.ncep.noaa.gov/data/indices/) Note that there are four 01 Nov start dates (for 1986, 1987, 2002 and 2015) which occur during a warm ENSO event, defined by having the Niño 3.4 index close to or above 1.0 for both forecast months. For the 01 Jan start dates, 1987, 1995 and 2010 corresponded to during warm events.

2.3 Data and diagnostics

The output of the 60-day forecasts includes the fields of temperature T, geopotential height Z, horizontal winds (u,v) and vertical pressure velocity ω at 12 pressure levels: $1000, 925, 850, 700, 600, 500, 400, 300, 250, 200, 100, 50\,hPa$. These fields were available twice-daily on an N80 Gaussian ($320^o \times 160^o$) lon x lat grid.

125   The diabatic heating was computed as a residual in the thermodynamic equation, with resolution equivalent to T159 in spherical harmonic space, following the algorithm described in Swenson and Straus (2021). While the output of the algorithm yields the heating in Wm^{-2} integrated over three layers: $1000-850\,hPa, 850-400\,hPa, 400-50\,hPa$, in this paper we only show the full vertical integral spanning $1000-50\,hPa$, which we refer to as Q. The daily mean diabatic heating from the ERA5 reanalysis (Hersbach and coauthors, 2020) was computed from the same fields, sampled four times per day, for the Novembers
130 of the eight years listed in Table 1.

    The effective barotropic Rossby wave source was computed following the prescription of Sardeshmukh and Hoskins (1988) as:

$$S = -\boldsymbol{\nabla} \cdot (\boldsymbol{v}_\chi \zeta) \tag{1}$$

where ζ is the absolute vorticity, and $\boldsymbol{v}_\chi$ the divergent component of the horizontal flow vector. This was evaluated at the 200
135 hPa level, using model fields at an equivalent T21 spectral truncation. The final result was also truncated to T21, and averaged over two-day blocks. In order to consider the source outside the deep tropics (where the background easterlies would suppress a stationary wave response) and in the vicinity of the sub-tropical jet, we consider the average source between 15^oN and 30^oN. The final values were divided by $\frac{2\Omega}{a}$, where Ω is the angular rotation rate of the earth, and a the radius of the earth. The scaled values have units of $\frac{m}{s}$.

2.4 Definition of anomalies

The seasonal cycles corresponding to the Nov. and Jan. MJO experiments listed in Table 1 are computed from the corresponding all-year experiments, and are characterized by a single climatological parabola in time for each variable and grid point, as in Straus (1983). Deviations in time about this seasonal cycle give the anomalies.

2.5 Metrics of uncertainty

145 Several metrics of the growth in uncertainty due to the small perturbations in the initial conditions are used in this paper. In all cases what is measured is the uncertainty due solely to the spread of each ensemble with forecast time, without any reference to reanalysis or observations. The *internal error variance* is defined as the average squared difference of a variable between the perturbed reforecasts and the control reforecast for the same initial date, and gives a measure of the "perfect model" error. The *ensemble error variance* is defined as the average of the squared difference between the perturbed reforecasts and the ensemble
150 mean. Its square root is referred to as the ensemble spread. Finally, the *external error variance* is defined as the average of the squared difference between each reforecast of one ensemble and all the control forecasts from the all-year experiments. The

external error variance gives a simple measure of the saturation level of the internal error variance. This saturation level will depend on time due to the evolution of the seasonal cycle.

3 Results

3.1 Tropical signal and noise

Although all eight (five) initial conditions for 1 Nov. (1 Jan.) for our experiments occur within MJO phases 2-3 (with a normalized amplitude greater than 1.0), the evolution of the tropical heating anomalies is quite variable from experiment to experiment. This is illustrated in Figure 1 (for the Nov experiments) and Figure 2 (for the Jan experiments). The daily averaged evolution of vertically integrated diabatic heating anomaly is shown averaged over the tropical band (15S-15N) and over all ensemble members and all four 01 Nov experiments during warm ENSO events (1986, 1987, 2002 and 2015) in Figure 1(a), and averaged over the four remaining 01 Nov experiments (1990, 2001, 2004 and 2011) in Figure 1(b). The average over all 8 Nov experiments is shown in Figure 1(c). The propagation of the heating corresponding to the MJO is seen clearly in each of the averages, but with a distinct difference. During non-ENSO years (Figure 1(b)), the diabatic heating envelope propagates from $90^o E$ to $120^o E$ in about 7 days and reaches the dateline by day 10. In contrast, during the warm ENSO years (Figure 1a) the main envelope of heating propagates slightly westward initially and then starts its eastward propagation only around day 6. A weaker secondary branch of heating is also seen propagating eastward around day 3. After day 10, the ENSO heating anomaly in the eastern Pacific dominates.The heating anomaly averaged over all experiments (Figure 1c) tends to wash out these two distinct signals.

For the January experiments, the non-ENSO years (Figure 2b) show a strong eastward moving envelope of heating which takes about 12 days to reach the western Pacific but then spreads rapidly to the dateline by around day 14. In the Indian Ocean, the eastward propagating envelope of heating consists of two westward propagating sub-branches. Strong westward propagation is also seen initiated in the eastern Pacific Ocean. The warm ENSO event average heating anomalies shown in Figure 2a are perhaps the most interesting: The Initially westward propagating envelope turns eastward around day 6 and then jumps to the eastern Pacific by day 9, with subsequent rapid propagation to join the main ENSO-related heating anomalies around $160^o W$. Meanwhile, a second MJO episode is seen to develop in the western Indian Ocean at day 10, propagating rapidly into the eastern Pacific. For the January experiments, the average over all experiments (Figure 2c) shows a distinct eastward propagating envelope, with westward propagating sub-components.

3.2 Tropical error growth

The daily averaged ensemble spread of vertically integrated heating Q, averaged over all November [January] experiments, is shown in Figure 1d [Figure 2d]. The spread develops quickly at the same longitude as the average heating anomalies, $80^o - 90^o E$ in November and $90^o E$ in January, but with a somewhat larger magnitude. Note that the color bar scale is different for the ensemble spread than for the anomalies. The heating spread grows substantially in the Indian Ocean during the November

experiment, as expected since the stochastic perturbations are applied this region. (Note that the longitudinal boundaries of the applied perturbations are indicated by the faint vertical red lines in Figure 1b.) In order to determine whether the strength of the stochastic perturbations (reflected in the magnitude of the ensemble spread in the Indian Ocean region) is reasonable, we also computed the the inter-annual standard deviation of the November Q from the ERA5 reanalysis over the eight years corresponding to the Nov. Experiment. Figure A1 in the Appendix shows the daily evolution of the standard deviation with the same scale as in Figure 1d. In the Indian Ocean region the two fields are comparable.

The spread in January, having developed quickly in the Indian Ocean, becomes (after day 10) intense at the eastern edge of perturbation region (around $120^{o}E$) following the average heating anomaly. For both cases, the spread also develops in the central Pacific, following to some extent the average heating.

In order to investigate the scale-dependence of the uncertainty of the heating evolution, we calculated the evolution of the internal, external and ensemble error variances of (two-day averaged) Q over the tropical belt $15^{o}S - 15^{o}N$. Since it is expected that very small-scale differences in Q will not contribute significantly to the global response, we have smoothed the heating by retaining only scales consistent with a T21 spherical harmonic representation prior to computing the error variances. The zonally averaged variances are decomposed into contributions due to groups of zonal wavenumber m. Figure 4a shows the evolution of the error variances of Q averaged over all Nov. experiments. The internal variance is shown by the black curves, the external error variance by the blue curves and the ensemble error variance by the red curves. Results are shown for various groups of zonal wavenumber: $1 - 3$ (top panel), $4 - 10$ (middle panel) and $11 - 21$ (lower panel). The results for the Jan. experiments are given in Figure 4b. The large-time limit of the internal error variance is seen to be about twice that of the ensemble error variance, as expected.

For the planetary waves ($m = 1 - 3$), the internal error stays well below our estimate of the external (or saturation) error for 30 days and beyond, but at this forecast range the saturation of the internal error is almost complete for $m = 4 - 10$. The internal error variance for smaller scales $m = 11 - 21$ reaches the external error variance prior to day 30. These observations hold for both Nov. and Jan. experiments, and also hold for the ensemble error variance, which particularly in the Nov. experiments is still growing, albeit slowly at day 60.

It is instructive to normalize the internal error variance shown in Figure 4 by the corresponding external error variance for each forecast time. The resulting normalized error variance (shown by the black lines in Figure 5) approach and hover about 1.0 at large times for all wavenumber groups except $m = 1 - 3$, for which the error does not appear to have saturated even at day 60. In order to summarize the error growth characteristics in a way which allows comparison between experiments, wave groups and variables, we define a *predictability time τ* as the time it takes for the normalized internal error to reach 0.5, as indicated by the light black horizontal lines in Figure 5. The rate of internal error growth vis-a-vis the external error (saturation) can then by summarized by the single measure τ, which allows for easy comparison between different variables and regions.

The predictability times for the vertically integrated heating Q (averaged $15^{o}S - 15^{o}N$) and the 200 hPa Rossby wave source S (averaged $15^{o}N - 30^{o}N$) are given in Table 3 for the three wavenumber groups and for both Nov. and Jan. reforecasts. The predictability time for the planetary wave Rossby wave source τ_S is considerably shorter than that for the heating τ_Q in

both Nov. (14 vs. 24 days) and Jan. (19 vs. 28 days). As the zonal scale decreases (larger m), τ generally decreases, and τ_S approaches τ_Q.

3.3 Global error growth

220 To get a sense of how the errors spread geographically, we present maps of the ensemble spread in vertically integrated heating Q for various forecast ranges up to day 30 in Figure 6 for the Nov. experiments, and in Figure 7 for the Jan. experiments. In November, the spread is largely confined to the Indo-Pacific region through days 5-6, begins to propagate into the northern hemispheric storm track regions by days 9-10, and by days 15-16 is well established in the North Pacific and Atlantic Oceans (and also the sub-tropical southern hemisphere oceans). Beyond forecast day 15, and up to Day 30, the errors intensify but

225 retain a similar distribution. The spread in heating in the Jan. experiments follow a similar evolution. However by Day 30 a noticeable hemispheric asymmetry is present, with much stronger errors in the southern hemisphere.

In considering the evolution of the ensemble spread of vorticity, we have retained only scales consistent with a T21 spherical harmonic representation, consistent with the treatment of heating.The evolution of the spread in vorticity at 200 hPa shown in Figures 8 and 9. It is clear that the vorticity ensemble error grows more quickly in the extratropics than the tropics. As with

230 the heating, the errors begin to propagate into mid-latitudes by forecast days 9-10 and are well established in the storm track regions of both hemispheres by days 15-16, after which they amplify. Noteworthy is the hemispheric asymmetry for Nov., with the northern hemisphere errors dominating at day 30.

3.4 Error propagation through the stratosphere

Since the stratosphere plays a dominant role in teleconnections from the tropics as a modulator for extratropical long-range

235 forecasts (e.g. Domeisen et al., 2015), we next evaluate the role of the stratosphere in error propagation. The ensemble error variance of the zonal wind u was integrated over the polar cap ($60^o N - 90^o N$), and the contributions to the zonal mean error variance from errors in the zonal flow and zonal wavenumbers $m = 1 - 3$ computed. The corresponding spread (square root of the variance) is shown in Figures 10a and 10b for the November initializations, and Figures 10c and 10d for January, at levels from $1000 - 50 hPa$. Some evidence for the downward propagation of errors (in the form of ensemble spread increasing from

240 the top, i.e. from $50 hPa$) from the stratosphere appears during the last 10 days of the November experiments, and slightly earlier in the January initializations, in both the zonal mean and planetary wave contributions. This downward propagation is potentially linked to wave-mean flow interaction which acts to bring anomalies in e.g. wind and temperature to the lower stratosphere. The planetary wave error in the upper troposphere ($300 hPa$) for Nov. reaches a maximum 20 days earlier than does the error at $50 hPa$, hinting at a tropospheric forcing of the stratospheric spread.

245 The upward propagation of the wave activity from the upper troposphere into the stratosphere, as measured by the vertical component of the Eliassen-Palm flux, is proportional to the zonal mean of the meridional eddy heat flux. Thus we would expect that if the spread in the tropospheric planetary wave activity is responsible for the growing ensemble error in the stratosphere, we should see evidence for this in the spread in the heat flux, especially in the contribution from zonal wavenumbers $m = 1 - 3$. Figure 11 shows this contribution as a function of time and pressure level for both Nov. and Jan. experiments. For Nov.,

250 enhanced spread in the eddy heat flux is seen by day 30, and by day 40 this spread has grown in the stratosphere. This occurs even earlier (by 10 days) in the Jan. experiments, likely due to the stronger wave flux into the stratosphere and hence a stronger upward coupling. For the Nov. experiments (Figure 11a), the spread increase in the upper troposphere is seen slightly prior to its increase in the stratosphere, although for the Jan. experiments the increased spread in the troposphere and stratosphere tends to occur nearly simultaneously.

255 In order to better understand the longitudinal dependence of the upward error growth, the geographical distribution of the planetary wave heat flux at 50 hPa is described in Figure 12. This figure shows both the ensemble mean eddy heat flux due to $m = 1 - 3$ and the ensemble spread, whose zonal mean is depicted in Figures 11a. and 11b. The four rows give pentad time averages for pentads 1, 3, 5 and 7. The heat flux itself is largely confined to the North Pacific in the ensemble mean, but other high latitude regions contribute substantially to the spread. This is true particularly for the Jan. experiments (columns 3 and 4), 260 in which large values of the spread are seen over the entire belt around $60^o N$ by pentad 5 (forecast days 21-25).

4 Discussion

The evolution of tropical heating averaged over all Jan. (Nov.) experiments in Figure 1c (2c) shows a strong maximum initially followed by eastward propagation with a reduced amplitude. The apparent decay of this average heating signal in time is due partly to the variation in the detailed evolution in the ensemble mean heating for the different initial dates. (Note that we also 265 have included one MJO phase-2 case for Jan., and two MJO phase-2 cases for Nov. in the grand average).

An indication of the variability among the ensemble members is the large ensemble spread of heating shown in Figures 1d and 2d. The very large initial uncertainty is confined to a narrow longitudinal range, but propagates in longitude with time as expected. In spite of this large local error in Q, the planetary wave component error grows much more slowly, with a predictability time τ_Q of 24 days for Nov. and 28 days for Jan. (Figures 4 and 5 and Table 3). In fact the planetary wave 270 internal error variance of Q does not fully saturate over the course of the experiments. The relatively long predictability times for tropical planetary wave heating are reflected in the predictability times for the tropical circulation as seen in Table 4, which are longer than their mid-latitude counterparts, consistent with earlier studies, for example Straus and Paolino (2009). Such long times justify the approach of, for example, Matthews et al. (2004) in using stationary wave concepts to describe the extratropical response to the MJO.

275 Although the largest scale heating and circulation components are predictable out to 3 weeks in these experiments, they do not directly force the extratropical response. Rather, the forcing is encapsulated in the Rossby wave source S. Since S is influenced not only by tropical and subtropical divergence but also by the meridional gradient of the jet, it is not as predictable as the heating (with τ reduced by about by 10 days, as seen in Table 3. This result indicates that one path by which mid-latitude and sub-tropical variability may affect the response to tropical forcing is by changing the effective source for that response. 280 The two-week predictability times for S are also consistent with the spread of vorticity and heating uncertainty to the storm track regions during that time, as seen in Figures 6,7,8 and 9.

The growth of uncertainty in the stratospheric circulation, as seen in Figure 10, is forced by the upward propagation of the planetary wave meridional flux of sensible heat (which is the dominant term in the vertical component of the Eliassen-Palm flux), shown in Figure 11. This uncertainty then propagates downward into the upper and middle troposphere. While most of the upper troposphere sensible heat flux is due to planetary wave disturbances in the Pacific, its uncertainty in the North Atlantic and Asian sectors are also large, especially for the Jan. experiments (Figure 12).

The stratospheric descent of error seen in Figure10 occurs towards the end of the experiments, consistent with the tropo­spherically forced uncertainty being modulated by the stratospheric circulation (Domeisen et al., 2020b). This descent is seen about 10 days later in the reforecast period for the Nov. experiments than for the Jan. experiments. This may be due to the lack of a fully formed stratospheric vortex during November, so that the establishment of a wave guide for vertically propagating Rossby waves is delayed. (It was not possible to verify this since data were retained only up to $50hPa$.)

5 Conclusions

The suite of reforecast ensemble experiments presented here was explicitly designed to gauge the effect of the uncertainty in the diabatic heating *within MJO phases 2 and 3* on the global circulation. We find that:

– The uncertainty (average ensemble spread) in total vertically integrated heating exceeds the signal, in part because the detailed evolution of the heating is case-dependent, especially with regard to the state of ENSO [Figures 1 and 2].

– The uncertainty of tropical heating is highly scale-dependent: the error on planetary scales has not fully saturated even at the end of the 60-day forecasts, whereas the small scales are fully saturated in about 30 days [Figure 5]. Reflecting this, the predictability time τ (defined by error reaching half its saturation level) for the planetary wave heating is between 24 and and 28 days [Table 3], whereas that for the small scale tropical heating is 14 days. The slow growth of errors in the planetary wave heating validates the application of stationary-wave theory to the extratropical response, as in Matthews et al. (2004)

– The predictability time τ for the tropical planetary scale vorticity is about 3 weeks, but is between 15 and and 19 days in mid-latitudes [Table 4].

– The predictability of the planetary wave component of the barotropic Rossby wave source is about 10 days less than that of the tropical heating, indicating that uncertainties in the gradients of planetary wave total vorticity are a factor in limiting extratropical predictability [Table 3].

– The role of the stratosphere in amplifying uncertainty is generally confined to the latter part of the 60-day reforecasts, after the ensemble spread in upper-tropospheric heat flux has affected levels above 50 hPa [Figures 10 and 11].

– Ensemble perturbations in both heating and vorticity generated over the tropical Indian Ocean amplify first within the tropical band and then propagate into the extratropics, reaching a noticeable amplitude over the North Atlantic after approximately 15 days, after which they amplify in situ during the following week [Figures 6 - 9]. Although estimates

of such a time lag were already available from observational studies (e.g. Cassou, 2008), the design of our experiments removes the uncertainty associated with the superposition of teleconnections from different parts of the tropical oceans.

315 *Code and data availability.* The data corresponding to the model fields mentioned in Section 2.3 are available by request to the authors, and reside at the Computational and Information Systems Laboratory (CISL) of the National Center for Atmospheric Research. Users are required to obtain a Data Analysis Allocation. More information is at : https://arc.ucar.edu/xras_submit/opportunities. The ERA5 reanalysis data are also available at CISL. The computer codes used to create Figs. 1 through 9 are written in Fortran, and were compiled a recent version of the Intel compiler. They are available from DMS by request.

320 *Author contributions.* The experiments were designed by FM and carried out by SJL, both of whom oversaw the data storage. DMS designed and carried out the analysis to create Figs. 1 through 9, while PY carried out the analysis for Figs. 10 through 12. DD wrote much of the Introduction, while DMS and SJL contributed to the remainder of the paper. All authors contributed to the discussion of the results and feedback on the manuscript.

Competing interests. The authors declare no competing interests.

325 *Acknowledgements.* Support from the Swiss National Science Foundation through project PP00P2_198896 to P.Y. and D.D. is gratefully acknowledged. The authors also acknowledge suggestions from Kai Huang, and helpful comments from Peter Dueben and Magdalena Alonso Balmaseda.

References

Baldwin, M. P. and Dunkerton, T. J.: Stratospheric harbingers of anomalous weather regimes, Science, 294, 581–584, 2001.

330 Buizza, R., Miller, M., and Palmer, T. N.: Stochastic representation of model uncertainties in the ECMWF ensemble prediction system, Q. J. R. Meteorol. Soc., 125, 2887–2908, https://doi.org/10.1002/qj.49712556006, 1999.

Camargo, S. J., Wheeler, M. C., and Sobel, A. H.: Diagnosis of the MJO modulation of tropical cyclogenesis using an empirical index, J. Atmos. Sci., 66, 3061–3074, 2009.

Camargo, S. J., Camp, J., Elsberry, R. L., Gregory, P. A., Klotzbach, P., Schreck, C. J., Sobel, A. H., Ventrice, M. J., Vitart, F., Wang, Z.,
335 Wheeler, M. C., Yamaguchi, M., and Zhan, R.: Tropical cyclone prediction on subseasonal time-scales., Trop. Cyclone Res. Rev., 8, 150–165, https://doi.org/10.1038/j.tccr.2019.10.004, 2019.

Cassou, C.: Intraseasonal interaction between the Madden-Julian Oscillation and the North Atlantic Oscillation, Nature, 455, 523 – 527, https://doi.org/10.1038/nature07286, 2008.

Dee, D. P. and coauthors: The ERA-Interim reanalysis: configuration and performance of the data assimilation system, Q. J. R. Meteor. Soc.,
340 137, 553–597, 2011.

Domeisen, D. I., White, C. J., Afargan-Gerstman, H., Muñoz, Á. G., Janiga, M. A., Vitart, F., Wulff, C. O., Antoine, S., Ardilouze, C., Batté, L., et al.: Advances in the subseasonal prediction of extreme events: Relevant case studies across the globe, Bulletin of the American Meteorological Society, 2022.

Domeisen, D. I. V., Butler, A. H., Fröhlich, K., Bittner, M., Müller, W. A., and Baehr, J.: Seasonal predictability over Europe arising from El
345 Niño and stratospheric variability in the MPI-ESM seasonal prediction system, Journal of Climate, 28, 256–271, 2015.

Domeisen, D. I. V., Butler, A. H., Charlton-Perez, A. J., Ayarzaguena, B., Baldwin, M. P., Dunn Sigouin, E., Furtado, J. C., Garfinkel, C. I., Hitchcock, P., Karpechko, A. Y., Kim, H., Knight, J., Lang, A. L., Lim, E.-P., Marshall, A., Roff, G., Schwartz, C., Simpson, I. R., Son, S.-W., and Taguchi, M.: The Role of the Stratosphere in Subseasonal to Seasonal Prediction: 2. Predictability Arising From Stratosphere-Troposphere Coupling, Journal of Geophysical Research-Atmospheres, 125, 1–20, 2020a.

350 Domeisen, D. I. V., Grams, C. M., and Papritz, L.: The role of North Atlantic-European weather regimes in the surface impact of sudden stratospheric warming events, Weather and Climate Dynamics, 1, 373–388, https://doi.org/10.5194/wcd-1-373-2020, 2020b.

ECMWF: IFS Documentation CY43R3, chap. Part V: Ensemble Prediction System, ECMWF, https://doi.org/10.21957/vk7qosxn5, 2017a.

ECMWF: IFS Documentation CY43R3, chap. Part VII: ECWMF wave model, ECMWF, https://doi.org/10.21957/mxz9z1gb, 2017b.

Ferranti, L., Palmer, T. N., Molteni, F., and Klinker, E.: Tropical-Extratropical Interaction Associated with the 30-60 Day Oscillation and
355 Its Impact on Medium and Extended Range Prediction, Journal of Atmospheric Sciences, 47, 2177 – 2199, https://doi.org/10.1175/1520-0469(1990)047<2177:TEIAWT>2.0.CO;2, 1990.

Garfinkel, C. I. and Schwartz, C.: MJO-Related Tropical Convection Anomalies Lead to More Accurate Stratospheric Vortex Variability in Subseasonal Forecast Models, Geophysical Research Letters, 44, 10,054–10,062, https://doi.org/10.1002/2017GL074470, 2017.

Garfinkel, C. I., Benedict, J. J., and Maloney, E. D.: Impact of the MJO on the boreal winter extratropical circulation, Geophysical Research
360 Letters, 41, 6055–6062, 2014.

Garfinkel, C. I., Chen, W., Li, Y., Schwartz, C., Yadav, P., and Thompson, Domeisen, D.: The Winter North Pacific Teleconnection in Response to ENSO and the MJO is Operational Subseasonal Forecasting Models is Too Weak, Journal of Climate, 35, 4413–4430, 2022.

Goosse, H. and Fichefet, T.: Importance of ice-ocean interactions for the global ocean circulation: A model study, Journal of Geophysical Research: Oceans, 104, 23 337–23 355, https://doi.org/10.1029/1999JC900215, 1999.

365 Hall, J. D., Matthews, A. J., and Karoli, D. J.: The modulation of tropical cyclone activity in the Australian region by the Madden-Julian Oscillation, Mon. Wea. Rev., 129, 2970–2982, 2001.

Hersbach, H. and coauthors: The ERA5 global reanalysis, Q. J. R. Meteorol. Soc., 146, 199 – 2049, https://doi.org/10.1002/qj.3803, 2020.

Jones, C., Waliser, D. E., Lau, K. M., and Stern, W.: Global Occurrences of Extreme Precipitation and the Madden?Julian Oscillation: Observations and Predictability, Journal of Climate, 17, 4575–4589, https://doi.org/10.1175/3238.1, 2004.

370 Lee, C.-Y., Camargo, S. J., Vitart, F., Sobel, A. H., and Tippett, M. K.: Subseasonal Tropical Cyclone Genesis Prediction and MJO in the S2S Dataset, Wea. Forecasting, 33, 967 – 988, https://doi.org/10.1175/WAF-D-17-0165.1, 2018.

Lee, R. W., Woolnough, S. J., Charlton-Perez, A. J., and Vitart, F.: ENSO Modulation of MJO Teleconnections to the North Atlantic and Europe, Geophysical Research Letters, 46, 13 535 – 13 545, https://doi.org/10.1029/2019GL084683, 2019.

Leroy, A. and Wheeler, M. C.: Statistical prediction of weekly tropical cyclone activity in the southern hemisphere, Mon. Wea. Rev., 136, 375 3637–3654, 2008.

Leutbecher, M., Lock, S.-J., Ollinaho, P., Lang, S. T. K., Balsamo, G., Bechtold, P., Bonavita, M., Christensen, H. M., Diamantakis, M., Dutra, E., English, S., Fisher, M., Forbes, R. M., Goddard, J., Haiden, T., Hogan, R. J., Juricke, S., Lawrence, H., MacLeod, D., Magnusson, L., Malardel, S., Massart, S., Sandu, I., Smolarkiewicz, P. K., Subramanian, A., Vitart, F., Wedi, N., and Weisheimer, A.: Stochastic representations of model uncertainties at ECMWF: state of the art and future vision, Q. J. R. Meteorol. Soc., 143, 2315–2339, 380 https://doi.org/10.1002/qj.3094, 2017.

Lin, H. and Brunet, G.: The influence of the Madden–Julian oscillation on Canadian wintertime surface air temperature, Monthly Weather Review, 137, 2250–2262, 2009.

Lin, H., Brunet, G., and Derome, J.: An Observed Connection between the North Atlantic Oscillation and the Madden-Julian Oscillation, Journal of Climate, 22, 364 – 380, https://doi.org/10.1175/2008JCLI2515.1, 2009.

385 Lin, H., Brunet, G., and Fontecilla, J. S.: Impact of the Madden-Julian Oscillation on the intraseasonal forecast skill of the North Atlantic Oscillation, Geophysical Research Letters, 37, https://doi.org/10.1029/2010GL044315, 2010.

Madden, R. A. and Julian, P. R.: Detection of a 40–50 day oscillation in the zonal wind in the tropical Pacific, Journal of Atmospheric Sciences, 28, 702–708, 1971.

Madden, R. A. and Julian, P. R.: Description of global-scale circulation cells in the tropics with a 40–50 day period, Journal of Atmospheric 390 Sciences, 29, 1109–1123, 1972.

Madec, G. and the NEMO team: NEMO ocean engine, Notes du Pôle de modẽlisation de l'Institut Pierre-Simon Laplace (IPSL), pp. 915–934, https://doi.org/10.5281/zenodo.1475234, 2013.

Maloney, E. D. and Hartmann, D. L.: Modulation of hurricane activity in the Gulf of Mexico by the Madden-Julian oscillation, Science, 287, 2002–2004, 2000.

395 Matthews, A. J., Hoskins, B. J., and Masutani, M.: The global response to tropical heating in the Madden-Julian oscillation during the northern winter, Q. J. R. Meteorol. Soc., 130, 1991 – 2011, https://doi.org/110.1256/qj.02.123, 2004.

Merryfield, W. J., Baehr, J., Batté, L., Becker, E. J., Butler, A. H., Coelho, C. A. S., Danabasoglu, G., Dirmeyer, P. A., Doblas-Reyes, F. J., Domeisen, D. I. V., Ferranti, L., Ilynia, T., Kumar, A., Müller, W. A., Rixen, M., Robertson, A. W., Smith, D. M., Takaya, Y., Tuma, M., Vitart, F., White, C. J., Alvarez, M. S., Ardilouze, C., Attard, H., Baggett, C., Balmaseda, M. A., Beraki, A. F., Bhattacharjee, P. S., 400 Bilbao, R., de Andrade, F. M., DeFlorio, M. J., Díaz, L. B., Ehsan, M. A., Fragkoulidis, G., Grainger, S., Green, B. W., Hell, M. C., Infanti, J. M., Isensee, K., Kataoka, T., Kirtman, B. P., Klingaman, N. P., Lee, J.-Y., Mayer, K., McKay, R., Mecking, J. V., Miller, D. E., Neddermann, N., Justin Ng, C. H., Osso, A., Pankatz, K., Peatman, S., Pegion, K., Perlwitz, J., Recalde-Coronel, G. C., Reintges, A.,

Renkl, C., Solaraju-Murali, B., Spring, A., Stan, C., Sun, Y. Q., Tozer, C. R., Vigaud, N., Woolnough, S., and Yeager, S.: Current and Emerging Developments in Subseasonal to Decadal Prediction, Bulletin of the American Meteorological Society, 101, E869–E896, 2020.

405 Muñoz, Á. G., Goddard, L., Mason, S. J., and Robertson, A. W.: Cross–time scale interactions and rainfall extreme events in southeastern South America for the austral summer. Part II: Predictive skill, Journal of Climate, 29, 5915–5934, 2016.

Rodney, M., Lin, H., and Derome, J.: Subseasonal Prediction of Wintertime North American Surface Air Temperature during Strong MJO Events, Monthly Weather Review, 141, 2897–2909, 2013.

Sardeshmukh, P. D. and Hoskins, B. J.: The generation of global rotational flow by steady idealized tropical divergence, Journal of the

410 Atmospheric Sciences, 45, 1228–1251, 1988.

Schwartz, C. and Garfinkel, C. I.: Troposphere-Stratosphere Coupling in Subseaslnal-to-Seasonal Models and its Importance for a Realistic Extratropical Response to the Madden-Julian Oscillation, Journal of Geophysical Research: Atmospheres, 125, e2019JD032 043, 2020.

Stan, C., Straus, D. M., Frederiksen, J. S., Lin, H., Maloney, E. D., and Schumacher, C.: Review of tropical-extratropical teleconnections on intraseasonal time scales, Reviews of Geophysics, 55, 902–937, 2017.

415 Stan, C., Zheng, C., Chang, E. K.-M., Domeisen, D. I., Garfinkel, C. I., Jenney, A. M., Kim, H., Lim, Y.-K., Lin, H., Robertson, A., et al.: Advances in the prediction of MJO-Teleconnections in the S2S forecast systems, Bulletin of the American Meteorological Society, 2022.

Straus, D. M.: On the role of the seasonal cycle, J. Atmos. Sci., 40, 303 – 313, 1983.

Straus, D. M. and Paolino, D.: Intermediate time error growth and predictability: tropics versus mid-latitudes, Tellus A, 61, 579 – 586, https://doi.org/10.1111/j.1600-0870.2009.00411.x, 2009.

420 Straus, D. M., Swenson, E., and Lappen, C.-L.: The MJO Cycle Forcing of the North Atlantic Circulation: Intervention Experiments with the Community Earth System Model, J. Atmos. Sci., 72, 660 – 681, https://doi.org/10.1175/JAS-D-14-0145.1, 2015.

Swenson, E. T. and Straus, D. M.: A modelling framework for a better understanding of the tropically-forced component of the Indian monsoon variability, J. Earth Syst. Sci., 130, https://doi.org/10. 1007/s12040-020-01503-z, 2021.

Valadão, C. E., Carvalho, L. M., Lucio, P. S., and Chaves, R. R.: Impacts of the Madden-Julian oscillation on intraseasonal precipitation over

425 Northeast Brazil, International Journal of Climatology, 37, 1859–1884, 2017.

Vitart, F.: Evolution of ECMWF sub-seasonal forecast skill scores, Q. J. R. Meteorol. Soc., 140, 1889 – 1899, https://doi.org/10.1002/qj.2256, 2014.

Vitart, F.: Madden-Julian Oscillation prediction and teleconnections in the S2S database, Q. J. R. Meteorol. Soc., 143, 2210–2220, 2017.

Vitart, F., Ardilouze, C., Bonet, A., Brookshaw, A., Chen, M., Codorean, C., Déqué, M., Ferranti, L., Fucile, E., Fuentes, M., et al.: The

430 subseasonal to seasonal (S2S) prediction project database, Bulletin of the American Meteorological Society, 98, 163–173, 2017.

Wang, J., Kim, H., Kim, D., Henderson, S. A., Stan, C., and Maloney, E. D.: MJO teleconnections over the PNA region in climate models. Part II: Impacts of the MJO and basic state, Journal of Climate, 33, 5081–5101, 2020.

Wheeler, M. C. and Hendon, H. H.: An All-Season Real-Time Multivariate MJO Index: Development of an Index for Monitoring and Prediction, Mon. Wea. Rev., 132, 1917 – 1932, https://doi.org/10.1175/1520-0493(2004)132<1917:AARMMI>2.0.CO;2, 2004.

435 Yadav, P. and Straus, D. M.: Circulation Response to Fast and Slow MJO Episodes, Monthly Weather Review, 145, 1577 – 1596, https://doi.org/10.1175/MWR-D-16-0352.1, 2017.

Table 1. Summary of the model runs performed for this study, for the November start dates (left) and the January start dates (right).

Start date	Ensemble size	Start date	Ensemble size
01 Nov 1986	50+1	01 Jan 1987	50+1
01 Nov 1987	50+1	01 Jan 1990	50+1
01 Nov 1990	50+1	01 Jan 1995	50+1
01 Nov 2001	50+1	01 Jan 2010	50+1
01 Nov 2002	50+1	01 Jan 2013	50+1
01 Nov 2004	50+1		
01 Nov 2011	50+1		
01 Nov 2015	50+1		
01 Nov 1981..2016	8+1	01 Jan 1981..2016	8+1

Table 2. Values of MJO amplitude and phase for the initial date of each reforecast ensemble, and observed monthly mean Niño 3.4 index for the two months of each reforecast ensemble. The index is only reported for absolute values above 1.0.

MJO Amplitude and Phase				
Start Date	MJO Amp	MJO Phase	Nino3.4 Nov	Nino3.4 Dec
01 Nov 1986	2.77	3	1.01	1.12
01 Nov 1987	1.58	2	1.07	
01 Nov 1990	1.76	3		
01 Nov 2001	1.56	3		
01 Nov 2002	1.96	2	1.47	1.37
01 Nov 2004	1.32	3		
01 Nov 2011	1.11	3	-1.19	-1.06
01 Nov 2015	2.04	3	2.72	2.66
Start Date	MJO Amp	MJO Phase	Nino3.4 Jan	Nino3.4 Feb
01 Jan 1987	1.22	2	1.14	1.13
01 Jan 1990	1.07	3		
01 Jan 1995	1.41	3	1.02	
01 Jan 2010	1.72	3	1.52	1.25
01. Jan 2013	1.07	3		

Table 3. Predictability Times based on normalized external error variance growth for vertically integrated heating averaged between $15^o S - 15^o N$, and 200 hPa Rossby wave source averaged between $15^o N - 30^o N$.

Tropical Predictability Times (days)				
wavenumb	Nov Heating	Nov RWS	Jan Heating	Jan RWS
1-3	24	14	28	19
4-10	18	14	20	16
11-21	14	12	14	14

Table 4. Predictability Times based on normalized external error variance growth for 200 hPa vorticity in the regions $15^o S - 15^o N$ ("Tropics") and $40^o N - 50^o N$ ("Mid-Lat").

Predictability Times (days)				
wavenumb	Nov Tropics	Nov Mid-Lat	Jan Tropics	Jan Mid-Lat
1-3	20	15	23	19
4-10	16	15	19	16
11-21	14	12	16	14
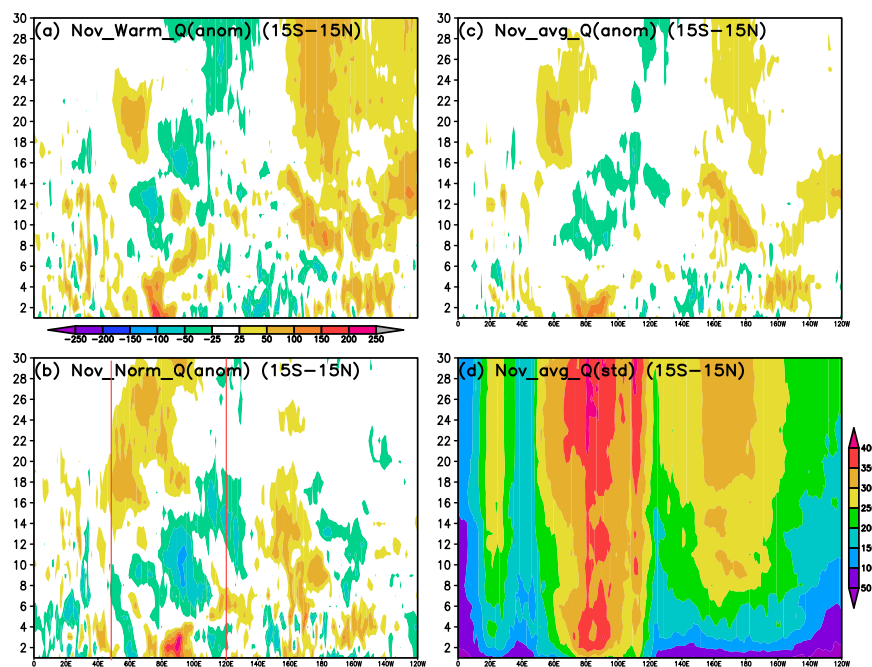
Figure 1. (a). Evolution of the daily mean, ensemble mean diabatic heating anomaly (vertically integrated and averaged 15S-15N) for days 1-30, averaged over the four Nov. experiments during warm ENSO events (1986, 1987, 2002 and 2015). (b) As in (a), but averaged over the four ENSO-neutral years (1990, 2001, 2004 and 2011). (c) As in (a), but for the average of all 8 Nov. experiments. (d). The evolution of the ensemble standard deviation of the daily mean heating (vertically integrated and averaged 15S-15N) averaged over all Nov. experiments. The color bar shown in panel (a) applies to panels (a)-(c). The red lines shown in the panel (b) indicate that range of longitudes over which the stochastic parametrization was applied. Units of Wm^{-2}.
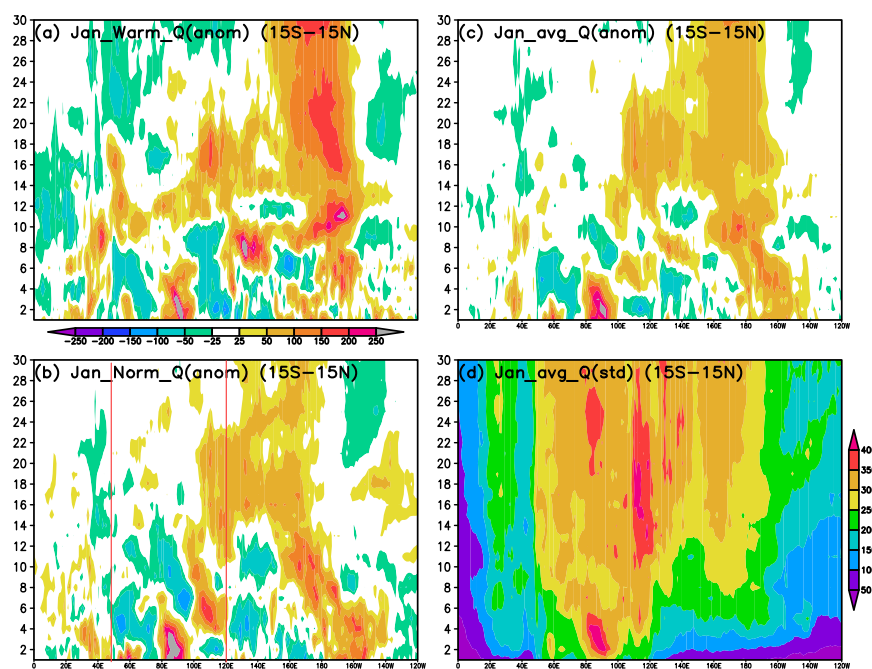
Figure 2. (a). Evolution of the daily mean, ensemble mean diabatic heating anomaly (vertically integrated and averaged 15S-15N) for days 1-30, averaged over the two Jan. experiments during warm ENSO events (1987 and 2010). (b) As in (a), but averaged over the three ENSO-neutral years (1990, 1995 and 2013). (c) As in (a), but for the average of all five Jan. experiments. (d). The evolution of the ensemble standard deviation of the daily mean heating (vertically integrated and averaged 15S-15N) averaged over all Jan. experiments. The color bar shown in panel (a) applies to panels (a)-(c). The red lines shown in the panel (b) indicate that range of longitudes over which the stochastic parametrization was applied. Units of Wm^{-2}.
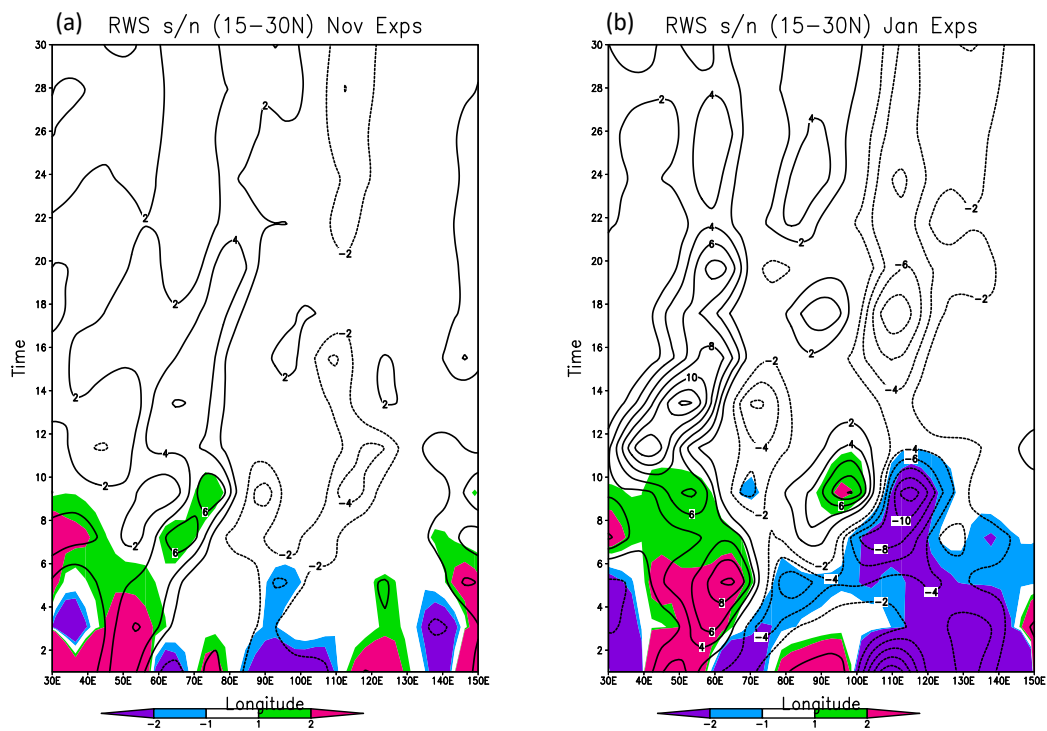
Figure 3. (a) Evolution of the Rossby Wave Source (RWS) averaged over the Nov. experiments. The RWS was computed using fields smoothed at the equivalent T21 triangular spectral truncation, and averaged between 15^oN and 30^oN. See text for details. The colors scale gives the ratio of the ensemble mean to ensemble spread. (b) Same as in panel (a), but for the Jan. experiments. The units of the RWS are ms^{-1}.
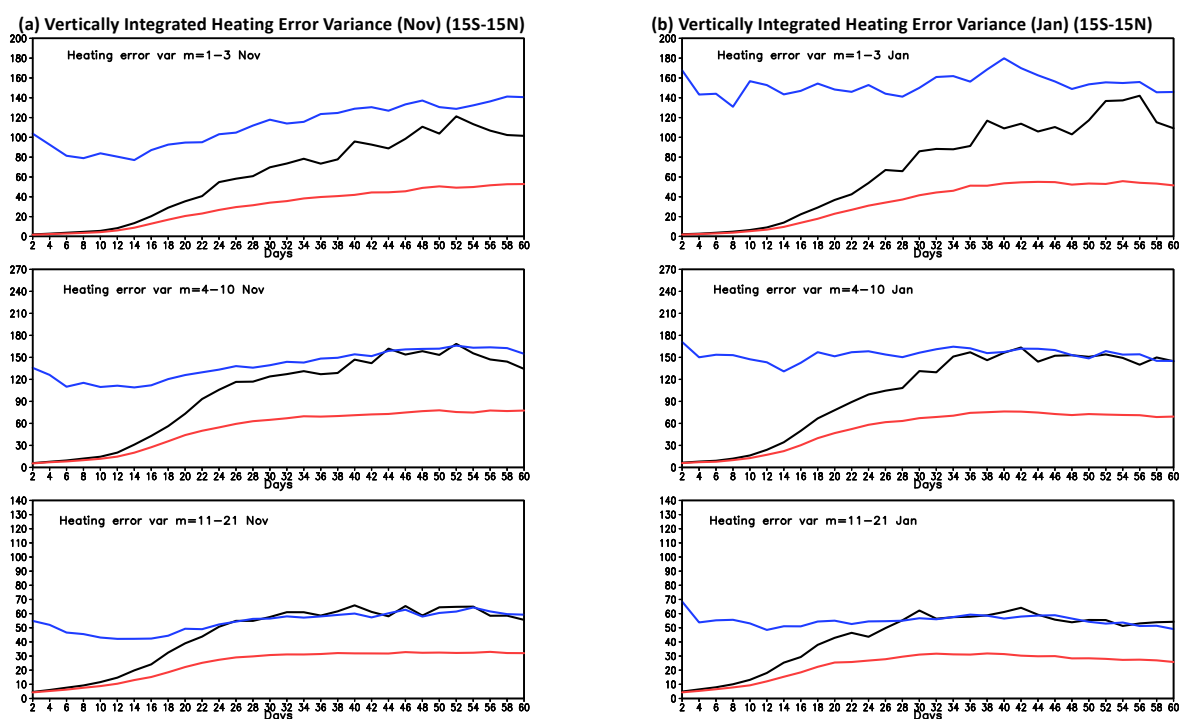
Figure 4. (a) Evolution of error variance of heating Q, truncated to a T21 representation, in various zonal wavenumber groups averaged over all Nov. experiments, averaged between 15S –15N. Top: zonal waves 1 – 3. Middle: zonal waves 4 – 10. Bottom: zonal waves 11 – 21. Solid red curves: Average variance about the ensemble mean. Solid black curves: Average error with respect to the control run of each ensemble. Solid blue curves: Average error with respect to control runs for many years (estimate of saturation error). (b) Same but for Jan. experiments. Units of $(Wm^{-2})^2$.
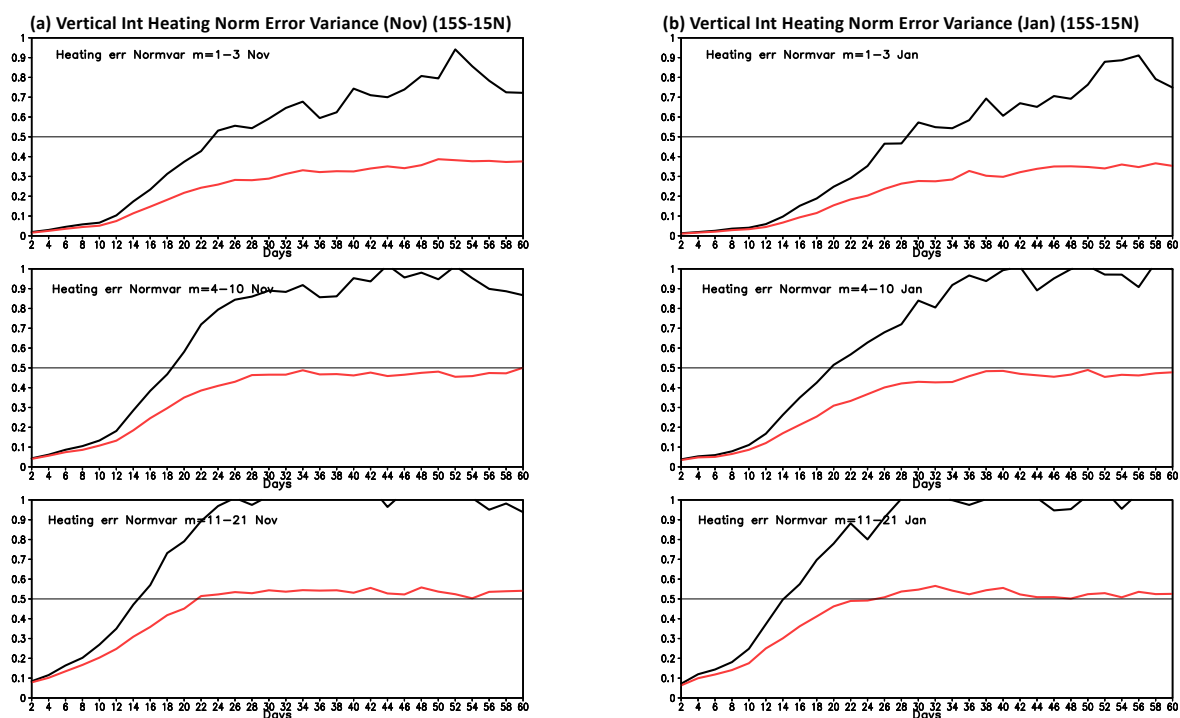
Figure 5. (a) Evolution of normalized error variance of heating Q, truncated to a T21 representation, in various zonal wavenumber groups averaged over all Nov. experiments, averaged between 15S – 15N. Top: zonal waves 1 – 3. Middle: zonal waves 4 – 10. Bottom: zonal waves 11– 21. Solid black curves: Average error with respect to the control run of each ensemble. Solid red curves: Average variance about the ensemble mean. Each curve is normalized by the saturation curve shown in Figure 4. (b) Same but for Jan. experiments. Units of $(Wm^{-2})^2$.
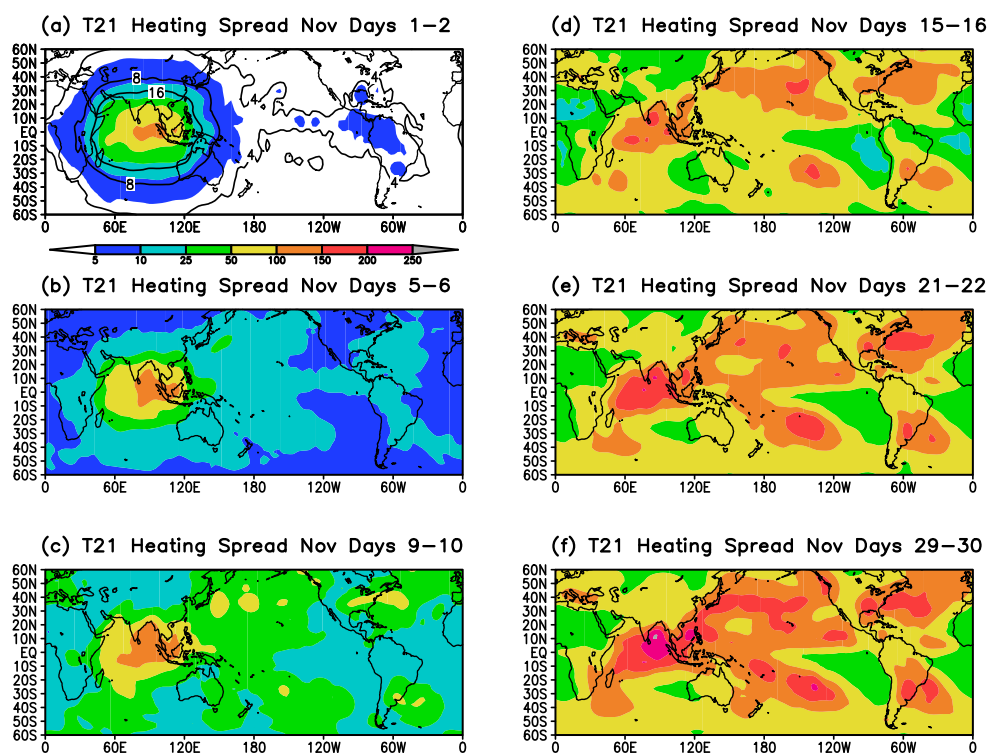
Figure 6. Ensemble spread of diabatic heating (vertically integrated) averaged over all Nov. experiments for various forecast ranges. Heating has been averaged over 2-day blocks and has been spatially filtered to retain only scales corresponding to T21 truncation. Units of Wm^{-2}. The color bar in panel (a) applies to all panels. Additional contours at 4,8 and 16 are indicated in panel (a).
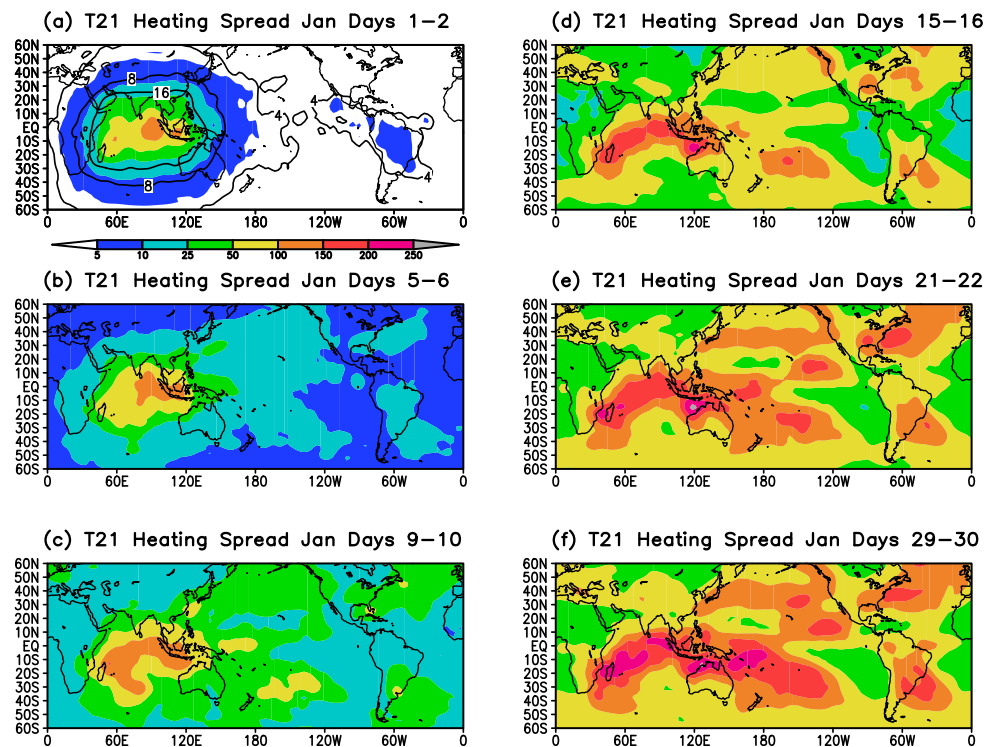
Figure 7. Ensemble spread of diabatic heating (vertically integrated) averaged over all Jan. experiments for various forecast ranges. Heating has been averaged over 2-day blocks and has been spatially filtered to retain only scales corresponding to T21 truncation. Units of Wm^{-2}. The color bar in panel (a) applies to all panels. Additional contours at 4,8 and 16 are indicated in panel (a).
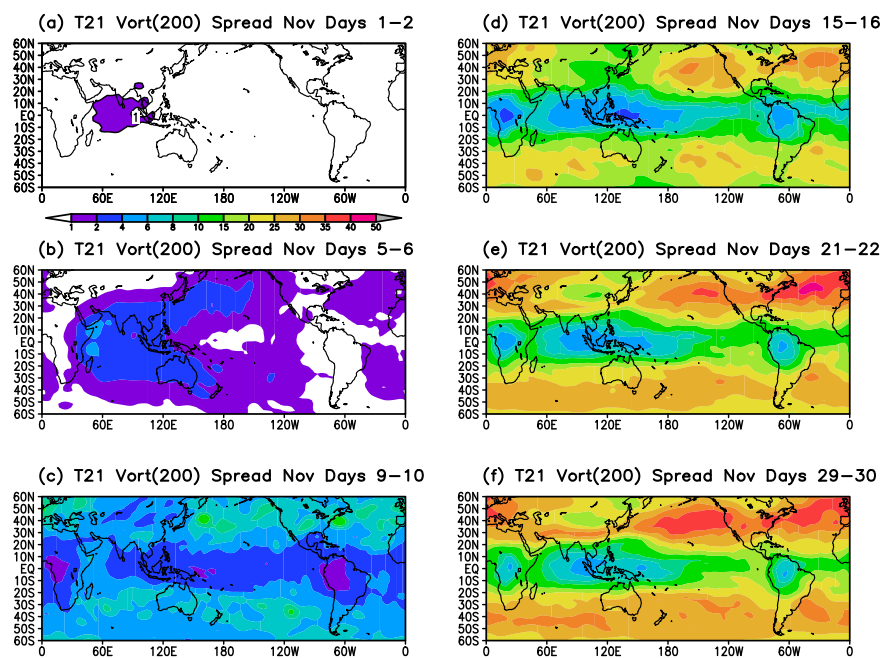
Figure 8. Ensemble spread of 200 hPa vorticity averaged over Nov. experiments for various forecast ranges. The vorticity has been averaged over 2-day blocks and has been spatially filtered to retain only scales corresponding to T21 truncation. Units of $10^{-6}s^{-1}$ The color bar in panel (a) applies to all panels.
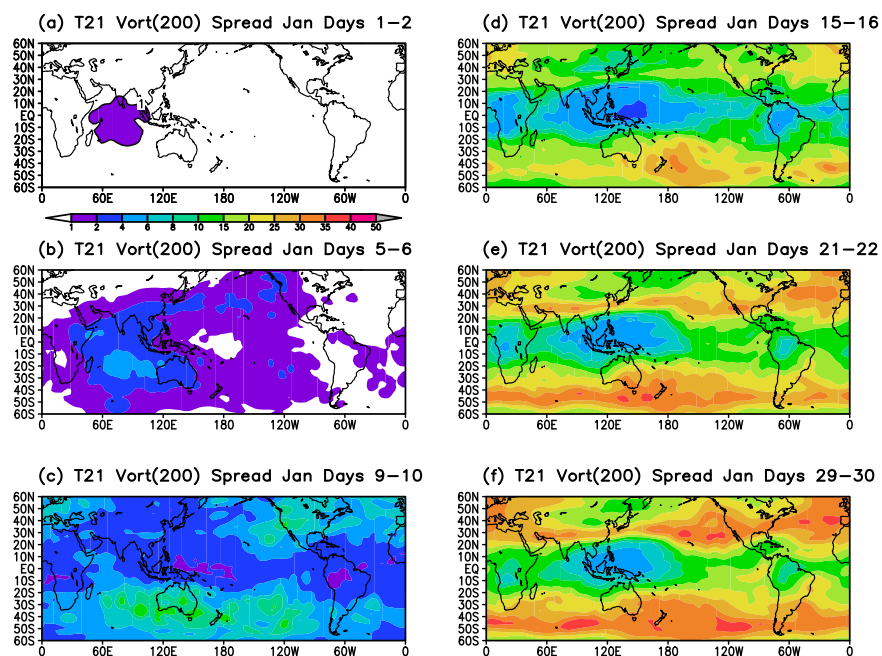
Figure 9. Ensemble spread of 200 hPa vorticity averaged over Jan. experiments for various forecast ranges. The vorticity has been averaged over 2-day blocks and has been spatially filtered to retain only scales corresponding to T21 truncation. Units of $10^{-6}s^{-1}$ The color bar in panel (a) applies to all panels.
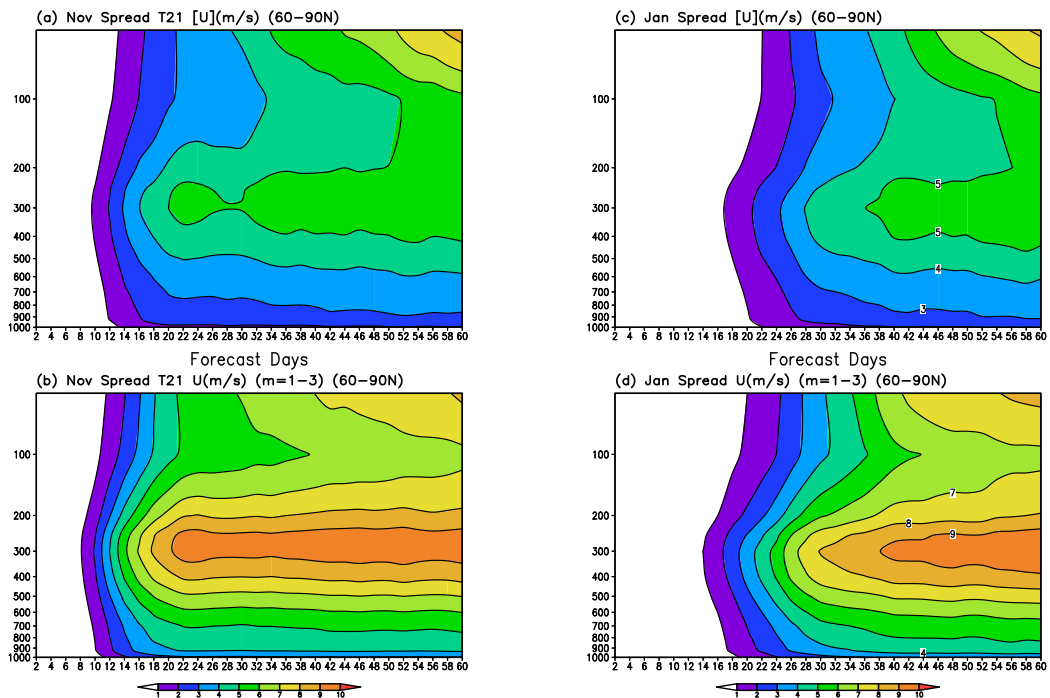
Figure 10. Ensemble spread of the zonal wind u, averaged 60N-90N for all levels (1000 - 50 hPa). The spread of the zonal-mean wind $[u]$ is shown in panels (a) and (c), and the spread due to zonal wavenumber 1-3 (panels (b) and (d)). The average spread over all Nov. experiments is shown in panels (a) and (b), over all Jan. experiments in panels (c) and (d). Units of ms^{-1}.)
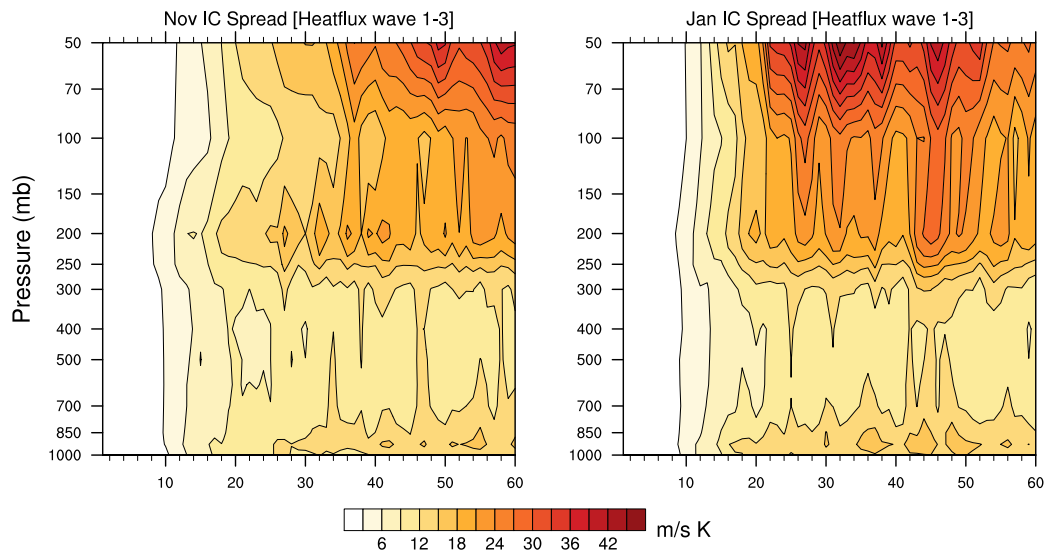
Figure 11. Ensemble spread for meridional eddy heat flux (summed over zonal wavenumbers 1 to 3) averaged between 40-80°N for Nov. (left) and Jan. (right) experiments. Units of $ms^{-1}K$.
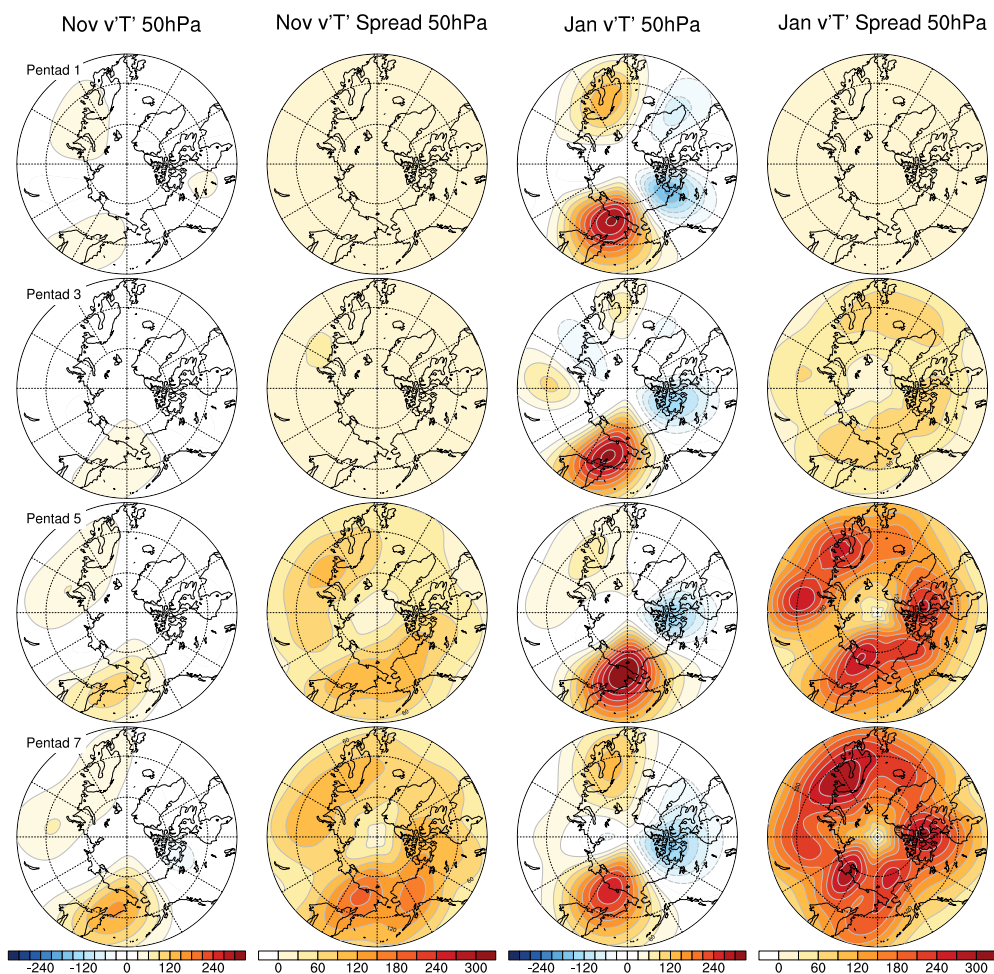
Figure 12. Geographical distribution of the planetary wave contribution to the zonal mean ensemble average and ensemble spread of meridional eddy heat flux at 50hPa. The ensemble average is shown in columns 1 and 3, the ensemble spread in columns 2 and 4 (as labeled). Rows 1 - 4 show averages over days 1-5, 11-15, 21-25 and 31-35 respectively. Nov. experiments are given in columns 1 and 2, Jan. results in columns 3 and 4. Contour interval is 30 $ms^{-1}K$.

Appendix
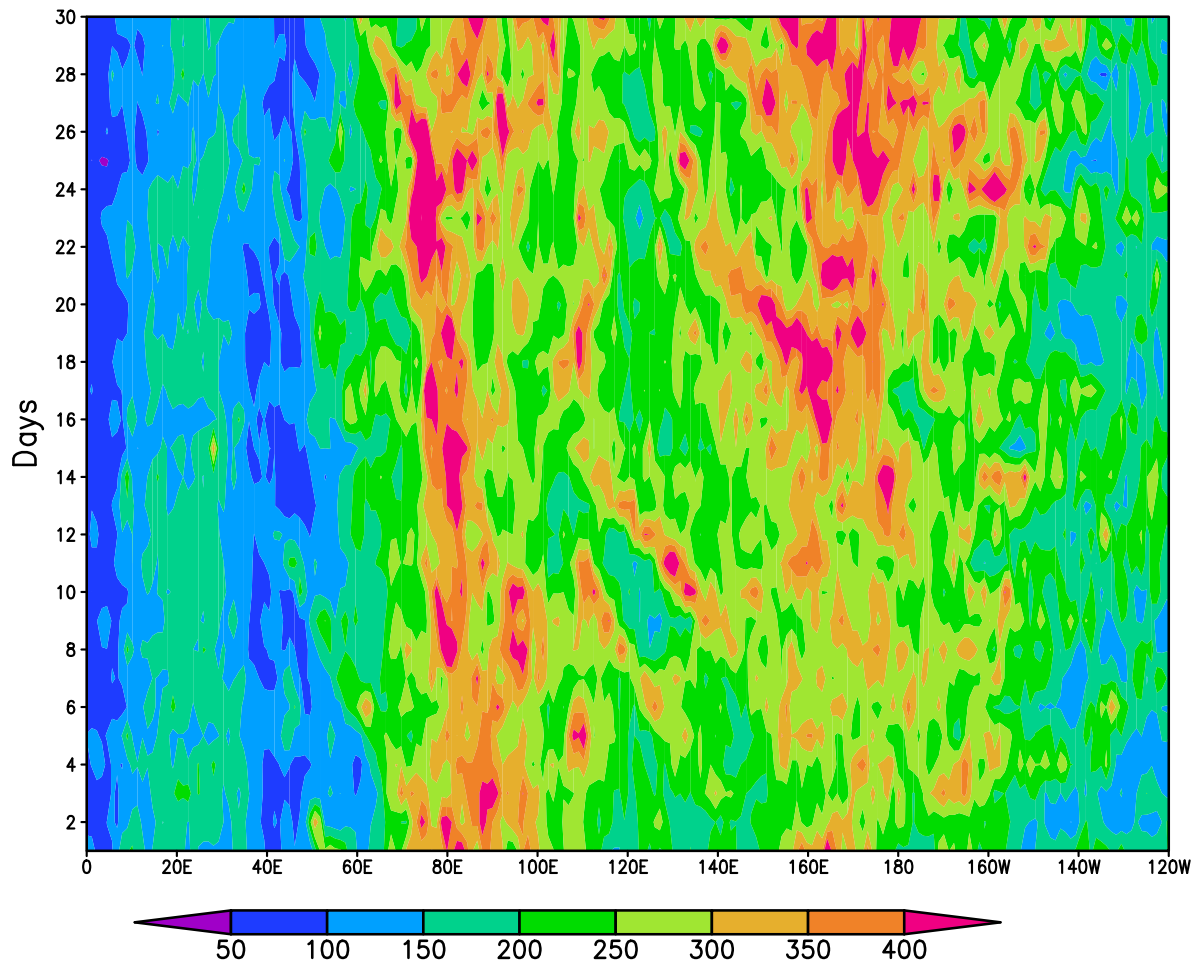
Figure A1. Variance of daily mean, vertically integrated diabatic heating (estimated from ERA5 reanalyses for days 1Nov to 30Nov) from the eight years corresponding to the Nov. experiments. See text for details. Units of Wm^{-2}.